

JOURNAL OF  
Optical Communications  
and Networking

# Ultra-high-capacity band and space division multiplexing backbone EONs: multi-core versus multi-fiber

FARHAD ARPANAEI,<sup>1,2,\*</sup> MAHDI RANJBAR ZEFREH,<sup>3</sup> CARLOS NATALINO,<sup>2</sup>   
 PIOTR LECHOWICZ,<sup>2</sup> SHUANGYI YAN,<sup>4</sup> JOSÉ M. RIVAS-MOSCOSO,<sup>5</sup>  
 ÓSCAR GONZÁLEZ DE DIOS,<sup>5</sup> JUAN PEDRO FERNÁNDEZ-PALACIOS,<sup>5</sup> HAMI RABBANI,<sup>6</sup>  
 MAITE BRANDT-PEARCE,<sup>6</sup> ALFONSO SÁNCHEZ-MACIÁN,<sup>1</sup> JOSÉ ALBERTO HERNÁNDEZ,<sup>1</sup>  
 DAVID LARRABEITI,<sup>1</sup> AND PAOLO MONTI<sup>2</sup>

<sup>1</sup>Department of Telematic Engineering, Universidad Carlos III de Madrid (UC3M), Leganés, Madrid, 28911, Spain

<sup>2</sup>Electrical Engineering Department, Chalmers University of Technology, 41296 Gothenburg, Sweden

<sup>3</sup>CISCO Systems S.R.L., Vimercate (MB), Italy

<sup>4</sup>Smart Internet Lab, University of Bristol, Bristol, UK

<sup>5</sup>Telefónica Global CTIO, S/N, 28050 Madrid, Spain

<sup>6</sup>Charles L. Brown Department of Electrical and Computer Engineering, University of Virginia, Charlottesville, Virginia 22904, USA

\*farhad.arpanaei@uc3m.es

Received 17 June 2024; revised 11 October 2024; accepted 14 October 2024; published 5 November 2024

Both multi-band and space division multiplexing (SDM) independently represent cost-effective approaches for next-generation optical backbone networks, particularly as data exchange between core data centers reaches the petabit-per-second scale. This paper focuses on different strategies for implementing band and SDM elastic optical network (BSDM EON) technology and analyzes the total network capacity of three sizes of backbone metro-core networks: ultra-long-, long-, and medium-distance networks related to the United States, Japan, and Spain, respectively. Two BSDM strategies are considered, namely, multi-core fibers (MCFs) and BSDM based on standard single-mode fiber (SSMF) bundles of multi-fiber pairs (BuMFPs). For MCF-based BSDM, we evaluated the performance of four manufactured trench-assisted weakly coupled (TAWC) MCFs with 4, 7, 13, and 19 cores. Simulation results reveal that, in the regime of ultra-low (UL) loss and inter-core crosstalk (ICXT), MCF-based throughput can be up to 14% higher than SSMF BuMFP-based BSDM when the core pitch exceeds 43  $\mu\text{m}$  and the loss coefficient is lower than that of standard single-mode fibers. However, increasing the number of cores with (non-)standard cladding diameters, UL loss, and ICXT coefficient is not beneficial. As core counts increase up to 13 for non-standard cladding diameters ( $<230 \mu\text{m}$ ), the core pitch and loss coefficient also increase, leading to degraded performance of MCF-based BSDM compared to SSMF BuMFP-based BSDM. The results indicate that, in scenarios with 19 MFPs, SSMF BuMFP-based BSDM outperforms 19-core MCF-based scenarios, increasing the throughput by 55% to 73%, from medium-backbone networks to ultra-long ones. © 2024 Optica Publishing Group. All rights, including for text and data mining (TDM), Artificial Intelligence (AI) training, and similar technologies, are reserved.

<https://doi.org/10.1364/JOCN.533086>

## 1. INTRODUCTION

The emergence of sixth generation (6G) mobile technology marks a pivotal moment in telecommunications, promising to overhaul high-speed, low-latency services by the anticipated horizon of 2030 [1]. This cutting-edge technology is motivated by an unprecedented surge in demand for bandwidth-intensive applications and services, compelling a substantial expansion in the capacity of the optical network infrastructure [2,3]. As novel technologies and applications that require greater

bandwidth continue to proliferate, Internet service providers and telecommunication operators (Telcos) face an urgent task: to increase their network capacity while also increasing cost-effectiveness and energy efficiency [4,5].

The integration of multi-band technology has emerged as a practical solution to meet these requirements [6,7]. However, projections suggest that by 2030, the developments of the 6G mobile communication landscape and the proliferation of artificial intelligence applications will demand a shift towards spatial multiplexing networks [2,8]. Developing a network

that seamlessly combines band and space division multiplexing (BSDM) technologies presents a complex task [9,10]. The challenges associated with few-mode fibers and few-mode multi-core fibers are considerable, rendering them unsuitable for long-haul and regional metro-core backbone networks [8]. To address these challenges while ensuring the stability of Telcos' infrastructure and compatibility with existing systems, recent studies have introduced weakly coupled multi-core fibers (MCFs) or bundles of multi-fiber pairs (BuMFPs) cables [11] for backbone optical networks.

Over the past 15 years, research on MCFs has led to the introduction of two categories: **strongly coupled (SC)** and **weakly coupled (WC)** [12,13]. In the case of SC fibers, multi-input multi-output (MIMO) digital signal processing (DSP) is required at the receivers, and the coupled channels must be treated as a single entity from the source to the destination; otherwise, regeneration at intermediate nodes becomes necessary [14]. The random coupling within SC-MCFs can mitigate the accumulation of non-linearity impairments, group delay differences between modes, spatial mode dispersion, and mode-dependent loss/gain. In this way, SC-MCFs could serve as promising candidates for long-haul point-to-point transmissions [14]. **In contrast, weakly coupled MCFs (WC-MCFs) do not require MIMO DSP at the receivers, and their channels can operate independently, allowing for optical switching without the need for optical-to-electrical-optical conversion/regeneration at intermediate nodes [15].** In terrestrial fully meshed regional/metro-core networks, WC-MCFs are preferred to circumvent the need for MIMO-DSP. **Due to these properties, this work focuses on WC-MCFs.** In recent years, various types of WC-MCFs have been introduced by both academia and industry, differing in core layout, number of cores, cladding diameters, thickness diameters, pitch distance, bandwidth, and other factors [13,14,16–19].

The WC-MCFs with hexagonally close-packed layout are regarded as the most spatially efficient, which is typically quantified in terms of the number of cores per unit area or volume. Three parameters are crucial in the manufacturing of WC-MCFs: **the core pitch, which is the distance between the centers of adjacent cores and affects inter-core crosstalk (ICXT); the cladding diameter (CD), closely related to the mechanical reliability of the optical fiber; and the cladding thickness (CT), which is the distance from the center of the outer core to the outer cladding edge affecting loss coefficients.** Designing WC-MCFs requires careful consideration of the number of cores within a limited cladding space [20]. While there is no standard cladding size for MCFs, a smaller diameter is preferable for achieving high core density and maintaining mechanical reliability during bending. **For practical use of WC-MCFs, suppressing ICXT is critical.** A smaller core pitch results in larger ICXT between adjacent cores, necessitating a decrease in effective area to reduce the coupling coefficient and, consequently, an increase in fiber non-linearity [21]. Additionally, the CT must be sufficient to reduce micro-/macro-bending losses in outer cores. Hence, there exists a trade-off relationship between ICXT, fiber non-linearity, and core density while maintaining a single-mode condition. The CD of WC-MCFs should be smaller than 230  $\mu\text{m}$  to satisfy the limit of failure probability, and the CT must be sufficiently

large ( $>40 \mu\text{m}$ ) for reducing micro-/macro-bending losses in outer cores [22].

In the course of this work, we consider these assumptions. The authors of [16] investigated WC-MCFs with a CD equivalent to that of traditional single-core fibers, typically 125  $\mu\text{m}$ . However, as mentioned earlier, in order to maintain low non-linearity, ICXT, and a low loss coefficient, the number of cores was set to 4, with a core pitch and cladding thickness greater than 40  $\mu\text{m}$  [19,23]. **Furthermore, in [24,25], the proposal of 6- to 8-core MCFs and 19-core MCFs, respectively, was noted; however, these WC-MCF configurations are not suitable for long-haul multi-band optical networks.** The intricacy of managing crosstalk becomes even more challenging in multi-band systems due to phenomena such as **inter-channel stimulated Raman scattering (ISRS), which notably affects the transmission quality and ICXT depending on the frequency [9].** Moreover, the frequency-dependent power coupling coefficient across different bands, unlike C-band systems, cannot be overlooked [9,26]. Recent advancements propose 4-core fibers of standard gauge for operation across all bands [21], with a core pitch of 43  $\mu\text{m}$  and a lower loss coefficient than standard single-mode fibers (SSMFs). In this study, we not only assess the performance of these fibers against non-standard cladding diameter fibers (less than 230  $\mu\text{m}$ ) but also compare ultra-low (UL)-ICXT MCF systems with single-mode BuMFPs. Additionally, determining the suitable operating range of MCFs based on the distance between adjacent cores and the trench width is critical [27,28]. This operating range ensures that ICXT resulting from core proximity does not compromise the bit rate of transceivers, relying solely on linear and non-linear noise factors to determine bit rates. This operating range is known as the UL-ICXT zone, where the modulation format level selection remains independent of ICXT. Consequently, network planning is less complex compared to ICXT-aware service provisioning, which is necessary for ICXT-sensitive WC-MCFs.

Today's network deployments adopt SSMFs due to their availability for the past several decades. However, optical networks need to be upgraded to meet the demands for ultra-wideband, high-capacity demands. Upgrading from SSMF (ITU-T G.652) to UL-loss (ULL) SMFs (ITU-T G.654) presents a significant opportunity for improving network performance in terms of reach and capacity [29–31]. ULL SMFs offer substantially lower attenuation compared to SSMFs, with loss coefficients ranging from 0.14 to 0.17 dB/km for ULL SMFs and from 0.19 to 0.22 dB/km for SSMFs at 1550 nm. This reduction in loss allows for extended transmission distances between amplification sites, effectively decreasing the number of amplifiers required across long-haul links. However, ULL SMFs might not be the only alternative. UL-loss-ICXT MCFs offer a higher spatial density within the same CD as standard SMFs, making them a compact and potentially more cost-effective option for greenfield deployments. Additionally, **in brownfield deployments, MCFs remain more efficient in terms of spatial density, especially due to the pre-established constraints in terms of space.** Therefore, UL-loss-ICXT MCFs may not yet surpass ULL SMFs in terms of loss coefficient, but their smaller footprint and potential for UL ICXT make them a promising alternative for ultra-wideband, high-capacity

networks. A fair comparison between UL-loss-ICXT MCFs and ULL SMFs should account for factors such as technological maturity, hardware availability, and long-term economic viability, but these studies are out of the scope of this paper. It is important to clarify that, throughout this work, when referring to BuMFP-based BSDM, we are specifically discussing its implementation using SSMF, and not ULL SMFs.

Additionally, the total network capacity exceeds that of WC-MCFs sensitive to ICXT. In ICXT-sensitive MCFs, the modulation format of each lightpath (LP) depends on the experienced ICXT [32]. In [33], the authors experimentally assessed the capacity performance of the C + L + S-band over a 3000 km 4-core SC-MCF with a cladding diameter of 125  $\mu\text{m}$ . While [34] proposed a survivable service provision algorithm for BSDM elastic optical networks (EONs) over the C + L-band, the linear noise of the QoT estimator did not model ISRS. Additionally, [10] experimentally evaluated the performance of 7-core and 4-core WC-MCFs over the C + L-band, revealing a wavelength dependence of ICXT in WC-MCFs, with nearly a 10 dB tilt between the short edge of the C-band and the long edge of the L-band for the considered fibers. Subsequently, [35] assessed the achievable throughput of C + L-band and S + C + L-band MCF transmission systems using fibers with standard cladding diameters, concluding that the optimal core count is 4, effectively balancing the effects of crosstalk with those of amplified spontaneous emission (ASE) and fiber non-linearity. In [36], the authors explore the evolution of optical networks, particularly the challenges related to optical signal switching in multi-band over SDM systems. While the work presents three novel node architectures, its focus remains on fiber-lane switching within BuMFPs rather than MCFs. Moreover, innovative approaches for transceivers and switching, focused on flexibility, energy efficiency, and sustainability, have been proposed to address the requirements of 6G optical networks. The study demonstrates multi-band over SDM technology, achieving up to 180.9 Gb/s transmission across the S + C + L-bands and validating a 19-core MCF scenario for next-generation network scalability and efficiency [37]. In [9], the authors also identify a critical wavelength where the influence of SRS on ICXT becomes negligible. Building on those findings, they proposed that, under the influence of SRS, arranging for low-frequency channels at low input power and high-frequency channels at high input power is advantageous for the design of BSDM EONs. Consequently, the HPO approach of employing flat receiver power, as proposed in our previous work [38], proves beneficial in achieving this objective. It is noteworthy that, to the best of our knowledge, this study is the first to consider this aspect, in contrast to existing literature such as [10,34].

In line with state-of-the-art studies, the contributions of this paper are as follows: (i) introducing a comprehensive analytical model for estimating the generalized signal-to-noise ratio (GSNR) for multi-band SDM EONs, inspired by the model proposed in [39]; (ii) analyzing the ICXT of WC-MCFs with standard and non-standard cladding diameters in different bands and cores for C + L + S-band systems; (iii) conducting a network-wide study of the performance of WC-MCFs with standard and non-standard cladding diameters, comparing them with C + L + S-band BuMFP BSDM in networks of

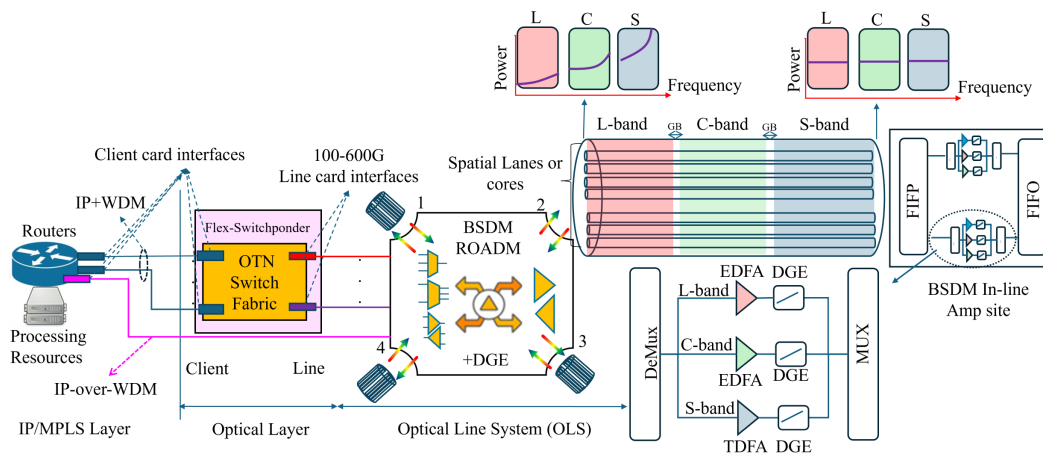
varying sizes; (iv) sharing the QoT profiles of all connections in the three sizes of networks in an open-source repository (see [40]) for use in future studies such as network planning, techno-economic analysis, and migration and upgrading studies from conventional/multi-band EONs to BSDM EONs. Simulation results reveal that MCF-based systems can outperform BuMFP-based BSDM by increasing the throughput by up to 14% in ultra-low ICXT and low-loss scenarios (MC04 and MC07) when the core pitch exceeds 43  $\mu\text{m}$  and the loss coefficient is lower than standard single-mode fibers. However, increasing the number of cores with non-standard cladding diameters ( $<230 \mu\text{m}$ ) leads to worse performance due to higher core pitch and loss coefficients. In scenarios with 19 MFPs, BuMFP-based BSDM outperforms 19-core MCF-based systems by 55% to 73% gains in throughput in medium to ultra-long networks.

The rest of this paper is structured as follows: Section 2 provides details of the system model for BSDM EONs, including node architectures and switching functionality. Section 3 describes the physical layer modeling for BSDM EONs, including a discussion on the linear, non-linear (Kerr and ISRS), and ICXT noises, which are essential for calculating the GSNR and ICXT. Section 4 introduces exhaustive simulation results and discussions on network capacity and ICXT analysis for different BSDM scenarios. Finally, Section 5 concludes this paper.

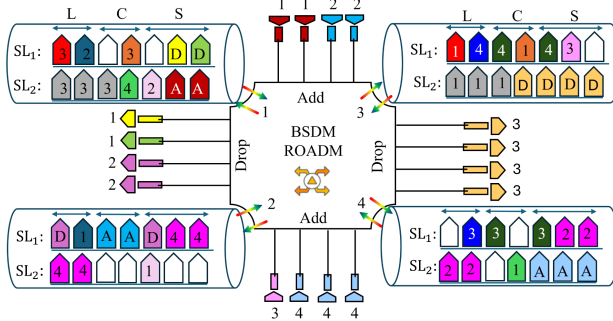
## 2. BAND AND SPACE DIVISION MULTIPLEXING EONS

Figure 1 shows the nodal architecture of BSDM EONs considered in this work. A multi-layer optical transport network (OTN) switching-based BSDM over WC-MCFs or BuMFPs is considered. The network uses C + L + S-band technology, providing approximately 20 THz of bandwidth. The modulation format of the line cards is tailored according to the GSNR [41]. Since the GSNR of each (channel, core) pair is different, due to the ISRS and ICXT in BSDM systems, the modulation format/transmission bit rate of each line card is contingent upon the channel and core utilized by the respective line card. For example, as shown in Fig. 2, the line card bit rate can vary from 100 Gbps to 600 Gbps. Therefore, the Internet protocol/multiprotocol label switching (IP/MPLS) traffic can be groomed via the OTN switch matrix and mapped to an idle line card that constructs an LP. However, the IP-over-WDM approach, which bypasses the optical terminal, would be another solution as illustrated in Fig. 1. Then, the LPs can be optically switched via a BSDM colorless, directionless, and contentionless (CDC) reconfigurable add-drop division multiplexer (ROADM) and transmitted through WC-MCFs/BuMFPs. For the sake of simplicity, we assume that switching the spatial lane (core/fiber) is not permitted.

The CDC BSDM ROADM is equipped with modules for telemetry, including optical channel monitoring (OCM), optical time-domain reflectometer (OTDR), and an optical supervisory channel (OSC) [42,43]. However, the optimal design for such an ROADM remains an open topic for future research. Proof-of-concept architectures and designs for various SDM ROADMs have been discussed in the literature, such



**Fig. 1.** Architecture of the nodes in BSDM EONs.



**Fig. 2.** BSDM CDC ROADM.

as in [44]. Additionally, it features a dynamic gain equalizer (DGE) to equalize the launch power and the pre- and post-amplifiers. The software-defined networking orchestrator oversees and regulates the routing, modulation format selection, grooming, spectrum assignment, and switching process based on the GSNR of each (channel, core) pair. The in-line amplifier sites of the BSDM are equipped with the DGE. Doped fiber amplifiers (DFAs) specific to each band and core amplify the signals at the in-line amplifying sites and in the CDC BSDM ROADM after the fan-in fan-out (FIFO) and the mux/demux components. Erbium-doped fiber amplifiers (EDFAs) are utilized in the C- and L-bands, while thulium-doped fiber amplifiers (TDFAs) are employed in the S-band. The DGEs are calibrated according to the hyper-accelerated power optimization (HPO) strategy proposed in [38].

In our study, we emphasize the concept of optimal flat received power at the end of each span as part of our HPO approach [38]. This technique is designed to enhance the capacity of multi-band optical systems by addressing the ISRS effects. The HPO approach involves adjusting the launch power of different frequency channels to compensate for the power loss experienced over the fiber span. Specifically, higher launch powers are applied to higher-frequency channels, which are more affected by ISRS. This adjustment aims to achieve a flat optical signal-to-noise ratio (OSNR) at the end of each span, facilitating effective network management and service monitoring. Although this results in a reduced tilt of the GSNR profile, it does not aim for a uniform GSNR profile,

which may not necessarily be optimal for maximizing span capacity. The benefits of this approach include improved network management through a consistent OSNR and a practical method for optimizing power in multi-band systems. The second benefit of this approach is accelerating power optimization, which is discussed in detail in [38]. However, it should be noted that, while the flat OSNR is maintained, the span capacity is optimized based on the adjusted power levels rather than a uniform GSNR profile. For a more comprehensive discussion on this technique and its impact on system performance, please refer to [38]. The in-line amplifier site architecture is proposed based on the discussion in [45]. However, the application of DGEs depends on the network scale.

The schematic diagram of the BSDM CDC ROADM is depicted in Fig. 2. The ROADM comprises four degrees, labeled as 1, 2, 3, and 4. Each LP is represented by different colors, with the LP's destination degree labeled from 1 to 4. For instance, the red LP is established between degrees 1 and 3 in the L-band of spatial lane 1 (SP1), while the yellow LP established on the link connected to degree 1 is dropped at a left-side line card. Since band and spatial lane switching is not allowed, no more pass-through LPs can be established at this node.

### 3. PHYSICAL LAYER MODELING FOR BSDM EONS

To mitigate crosstalk and enhance core density in MCFs, trench-assisted WC-MCFs (TAWC-MCFs) have been introduced. Figure 3 illustrates a representative cross-sectional view of a fabricated TAWC-MCF featuring a homogeneous core arrangement; i.e., the identical cores with a low-index trench profile are arranged in a hexagonal/square configuration. As depicted in the figure, a trench area with a lower relative refractive index ( $\Delta_2$ ) compared to the cladding is considered around each core, with a width of  $W_{tr}$ . The ICXT in TAWC-MCFs depends on fiber parameters such as the relative refractive index difference between the trench and cladding, trench width, and core pitch ( $r_1$ ). It also depends on the frequency, but this component is negligible in C-band optical networks. However,

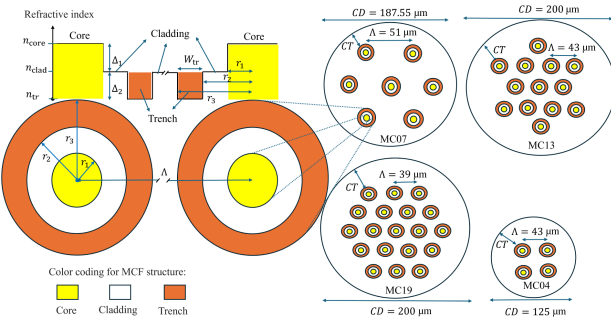


**Fig. 3.** Trench-assisted weakly coupled multi-core fiber layout: 7-core fiber (MC07) with a cladding diameter of 187.5  $\mu\text{m}$ , 13-core fiber with a cladding diameter of 200  $\mu\text{m}$ , 19-core fiber with a cladding diameter of 200  $\mu\text{m}$ , and 4-core fiber with a cladding diameter of 125  $\mu\text{m}$ .

as shown later, it is not negligible in multi-band systems like the C + L + S-band technology considered in this work.

In this study, we consider four different TAWC-MCF variants, each representing a specific cutting-edge technology: 1) MC04 with 4 cores and standard CD, i.e., 125  $\mu\text{m}$ ; 2) MC07 with 7 cores and non-standard CD, i.e., 181  $\mu\text{m}$ ; 3) MC13 with 13 cores and non-standard CD, i.e., 225  $\mu\text{m}$ ; and 4) MC19 with 19 cores and non-standard CD, i.e., 225  $\mu\text{m}$ . We have chosen these types of MCFs to not only compare the capacity performance of TAWC-MCFs with standard CD against those with non-standard CD, but also to evaluate the impact of increasing the number of cores in non-standard CD TAWC-MCFs on network capacity performance. Further details will be discussed in Section 4. All TAWC-MCFs have been fabricated in real-world scenarios.

To estimate the ICXT of TAWC-MCFs, several works in the literature proposed numerical simulations and experimental measurements [32,46,47]. Moreover, the authors of [27] proposed an analytical closed-form model for the mode coupling coefficient of the TAWC-MCFs. In this context, the ICXT of a TAWC-MCF can be calculated from Eqs. (1)–(3).

$$\mu_{\text{ICXT}}(f^i) = \frac{N_{\text{AC}} - N_{\text{AC}} \exp[-(N_{\text{AC}} + 1)\Omega(f^i)L]}{1 + N_{\text{AC}} \exp[-(N_{\text{AC}} + 1)\Omega(f^i)L]}. \quad (1)$$

The power coupling coefficient (PCC), denoted as  $\Omega(f^i)$  in Eq. (1), is calculated from Eq. (2), where  $\kappa$ ,  $r_b$ ,  $c$ ,  $\Lambda$ ,  $L$ ,  $n_{\text{core}}$ ,  $f^i$ , and  $N_{\text{AC}}$  represent the mode coupling coefficient (MCC), bending radius, propagation velocity, the distance between the centers of two adjacent cores (or core pitch), transmission distance, effective refractive index of the core, the channel's center frequency, and the number of lit adjacent cores of the channel under test, respectively.

$$\Omega(f^i) = \frac{c(\kappa(f^i))^2 r_b n_{\text{core}}}{\pi f^i \Lambda}. \quad (2)$$

Moreover, the MCC, denoted as  $\kappa$  in Eq. (2), is calculated from Eq. (3) [27]:

$$\kappa(f^i) \cong \frac{\sqrt{\Gamma \Delta_1}}{r_1} \frac{U_1^2(f^i)}{V_1^3(f^i) K_1^2(W_1)} \frac{\sqrt{\pi r_1}}{W_1 \Lambda} \\ \times \exp \left\{ -\frac{W_1 \Lambda + 1.2 [1 + V_1(f^i)] w_{\text{tr}}}{r_1} \right\}, \quad (3)$$

where

$$\Gamma = \frac{W_1}{W_1 + \frac{1.2(1+V_1(f^i))w_{\text{tr}}}{\Lambda}}$$

and

$$V_1(f^i) = \frac{2\pi f^i r_1 n_{\text{core}} \sqrt{2\Delta_1}}{c}, \quad K_1(W_1) = \sqrt{\frac{\pi}{2W_1}} e^{-W_1},$$

$$U_1^2(f^i) = \left[ \frac{2\pi f^i r_1}{n_{\text{core}} c} \right]^2 (n^4 - 1), \quad W_1|_{\frac{\Delta_1}{\Delta_1} = 2} = 1.143 V_1(f^i) - 0.22.$$

It should be noted that many works in the literature consider the PCC at 1550 nm, disregarding the dependency of the PCC and MCC on frequency, which affects the ICXT analysis in SDM-EONs [34,48–54]. For BSDM-EONs, the frequency dependency of the PCC and MCC is not negligible and must be taken into account. Therefore, the end-to-end QoT of an LP in terms of the GSNR at channel  $i$  is estimated from Eq. (4) inspired from the incoherent Gaussian noise (GN)/enhanced GN (EGN) model for multi-band systems proposed in [55]. Indeed, in this paper, we utilize the semi-closed EGN model presented in [39,55], which incorporates state-of-the-art techniques. This model is a GN/EGN model based on machine learning (ML), validated through both the split-step Fourier method and experimental testing [56–58].

$$\begin{aligned} & \text{GSNR}_{\text{LP}}^i|_{\text{dB}} \\ &= 10 \log_{10} \left[ (\text{SNR}_{\text{ASE}}^{-1} + \text{SNR}_{\text{NLI}}^{-1} + \text{SNR}_{\text{ICXT}}^{-1} + \text{SNR}_{\text{TRx}}^{-1})^{-1} \right] \\ &\quad - \sigma_{\text{Flt}}|_{\text{dB}} - \sigma_{\text{Ag}}|_{\text{dB}}, \end{aligned} \quad (4)$$

where  $\text{SNR}_{\text{ASE}} = \sum_{s \in S} P_{\text{tx}}^{s+1,i} / P_{\text{ASE}}^{s,i}$ ,  $\text{SNR}_{\text{NLI}} = \sum_{s \in S} P_{\text{tx}}^{s+1,i} / P_{\text{NLI}}^{s,i}$ , and  $\text{SNR}_{\text{ICXT}} = \sum_{s \in S} P_{\text{tx}}^{s+1,i} / P_{\text{ICXT}}^{s,i}$ . Moreover,  $P_{\text{tx}}^{s+1,i}$  is the launch power at the beginning of span  $s + 1$ ,  $P_{\text{ASE}}^{s,i} = n_f h f^i (G^{s,i} - 1) R_{\text{ch}}$  is the noise power caused by the DFA equipped with the DGE, and the non-linear interference (NLI) noise power ( $P_{\text{NLI}}^{s,i}$ ) is calculated from Eq. (5) [39]. In Eq. (5),  $n_f$ ,  $h$ ,  $f^i$ ,  $G^{s,i} = P_{\text{tx}}^{s+1,i} / P_{\text{tx}}^{s,i} S$ , and  $R_{\text{ch}}$  are the noise figure of the DFA, Plank's coefficient, the channel frequency, the frequency center of the spectrum, the gain of the DFA, the set of spans, and the channel symbol rate, respectively. Here,  $f_0$  denotes the frequency reference, which is associated with the wavelength 1550 nm, where  $\beta_2$ ,  $\beta_3$ , and  $\beta_4$  are measured. It should be noted that, without loss of generality, we assume the channel bandwidth and the symbol rate are identical.  $P_{\text{rx}}^{s,i}$  is the received power at the end of span  $s$ .  $\text{SNR}_{\text{TRx}}$ ,  $\sigma_{\text{Flt}}$ , and  $\sigma_{\text{Ag}}$  are the transceiver SNR, SNR penalty due to wavelength selective switch filtering, and SNR margin due to aging, respectively. Hence, the GSNR for all potential

connections from arbitrary sources to destinations in the network can be computed. Subsequently, the generalized mutual information (GMI) profiles of the K shortest (path, channel, core) tuples are pre-calculated, employing GSNR thresholds for each GMI [41].

$$P_{\text{NLI}}^{s,i} = \frac{16}{27} P_{\text{tx}}^{s+1,i} \sum_{\substack{1 \leq n \leq N_c, \\ 0 \leq j \leq 1, \\ 0 \leq k \leq M, \\ 0 \leq q \leq M}} \frac{\rho_n (\gamma^{i,n})^2 (P_{\text{tx}}^{s+1,n})^2 (2 - \delta_{i,n})(-1)^j e^{-4\alpha_1^n/\sigma^n}}{2\pi (R_{cb}^n)^2 k! q! (4\alpha_0^n + (k+q)\sigma^n) \bar{\beta}_2^n} \left( \frac{2\alpha_1^n}{\sigma^n} \right)^{k+q} \psi_{i,n,j,k}, \quad (5)$$

where

$$\gamma^{i,n} = \frac{2\pi f^i}{c} \frac{2n_{\text{core}}}{A_{\text{eff}}(f^i) + A_{\text{eff}}(f^n)},$$

and

$$\begin{aligned} \bar{\beta}_2^n &= \beta_2 + \pi \beta_3 (f^i + f^n - 2f_0) + \frac{2\pi^2}{3} \\ &\times \beta_4 \left[ (f^i - f_0)^2 + (f^i - f_0)(f^n - f_0) + (f^n - f_0)^2 \right], \\ M &= \text{MAX} \lfloor 10 \times |2\alpha_1^i/\sigma^i| \rfloor + 1. \end{aligned}$$

In multi-band WDM systems with a bandwidth exceeding 6 THz (super C-band), the gain/loss power profile for a pre-tilt-launch power scenario cannot be determined using a closed-form formula due to the need to solve the associated Raman ordinary differential equations (ODEs) [55]. Assuming  $N_{\text{ch}}$  channels having center frequencies  $f_1 < f_2 < \dots < f_{N_{\text{ch}}}$ , the evolution of power over distance for each channel is governed by a system of coupled differential equations:

$$\frac{\partial P_{\text{tx}}^{l,s,i}(z)}{\partial z} = \kappa P_{\text{tx}}^{l,s,i}(z) \left[ \sum_{n=1}^{N_{\text{ch}}} \zeta \left( \frac{f_i}{f_n} \right) C_r(f_n, f_n - f_i) P(f_n, z) - \alpha(f_i) \right], \quad I \in [1, N_{\text{ch}}], \quad (6)$$

where  $z$  is the signal propagation distance,  $\alpha(f_i)$  is the fiber attenuation at frequency  $f_i$ ,  $P_{\text{tx}}^{l,s,i}(z)$  is the power of the  $i$ th channel at distance  $z$ , and  $\kappa$  is set to +1 for a signal propagating along the  $+z$  direction (forward propagating), while  $\kappa = -1$  for signals propagating in the  $-z$  direction (backward propagating).  $\zeta(x)$  returns  $x$  for  $x > 1$ , 0 for  $x = 1$ , and 1 for  $x < 1$ .  $C_r$  exhibits odd symmetry with respect to the frequency difference  $\Delta f = f_n - f_i$ . This variable characterizes the gain profile of the Raman effect within the fiber. It is contingent on the fiber's physical attributes, such as the Raman gain coefficient and the effective area of the fiber. Additionally, we estimate the auxiliary loss coefficient profiles, i.e.,  $\alpha_0^i$ ,  $\alpha_1^i$ , and  $\sigma^i$ , by fitting the power evolution profile obtained from Eq. (6) and the approximately closed-form Formula (13) in [55]. The inspired actual frequency-dependent fiber loss can be loosely modeled based on Eq. (7):

$$\alpha(z, f^i) = \alpha_0(f^i) + \alpha_1(f^i) \exp\{-\sigma(f^i)z\}, \quad (7)$$

where  $z$  is the signal propagation distance, and the index  $i$  denotes the channel's frequency  $f^i$ . Indeed, the interpretation of Eq. (7) suggests that the observed loss coefficient in MB systems differs from the loss coefficient utilized in C-band systems. In this context,  $\alpha_0^i$  represents the fiber loss in the

absence of ISRS, while  $\alpha_1^i$  quantifies the loss alteration attributable to ISRS at the onset of the span. Additionally,  $\sigma^i$  characterizes the rate at which ISRS diminishes along the span with the decreasing optical power. Once these parameters are assigned, the NLI calculation becomes closed-form. However, assigning auxiliary loss coefficient profiles is not closed-form, as doing it in full closed-form would introduce excessive errors. This step is the only non-closed-form, being a semi-CFM QoT estimation approach. Equations (30.1) and (30.2) in [55] offer a closed-form best-fit for  $\alpha_1^i$  and  $\alpha_0^i$  given  $\sigma^i$ . Finally, optimizing numerically over  $\sigma^i$  gives the overall best-fit for  $\alpha_1^i$ ,  $\alpha_0^i$ , and  $\sigma^i$ . To calculate the power of ICXTs due to the coupling of adjacent cores for MCF, we can apply Eq. (8):

$$P_{\text{ICXT}}^{s,i} = \mu_{\text{ICXT}}^{s,i} P_{\text{tx}}^{s+1,i}. \quad (8)$$

A BSDM-EON over MCFs does not need the MIMO-DSP-equipped transceivers when the accumulated ICXT penalty on the SNR is equal to or lower than 1 dB [15,32,59]. The ICXT threshold of each modulation format in terms of acceptable bit error rate (BER) according to the corresponding GSNR ( $G_{\text{th}}$ ) in dB based on Eq. (9) is as follows:

$$\mu_{\text{ICXT}_{\text{th}}}^m = 10 \log_{10} \left( \frac{1 - 10^{\left(\frac{-\Gamma}{10}\right)}}{\chi^m \times 10^{\left(\frac{G_{\text{th}}}{10}\right)}} \right), \quad (9)$$

where  $\mu_{\text{ICXT}_{\text{th}}}^m$  is the threshold of acceptable ICXT of modulation format  $m$  for a given QoT penalty  $\Gamma = 1$  dB and BER. Additionally,  $\chi^{m=1}$  to  $\chi^{m=6}$  equal 0.5, 1, 3.41, 5, 10, 21 [32].

## 4. SIMULATION SETUP AND NUMERICAL RESULTS

Initially, we present a study on the TAWC-MCFs. Subsequently, we analyze the network performance for the two SDM scenarios, i.e., MCFs and BuMFPs.

**Table 1.** Physical Parameters of the Optical Fibers

Parameter	Symbol	MC04	MCF07	MC13	MC19	SSMF
Core counts	$n_c$	4	7	13	19	1
Cladding diameter [μm]	CD	125	187.5	200	200	125
Cladding thickness [μm]	CT	40	40	35	30	40
Core radius [μm]	$r_1$	4.5	4.5	4.1	3.6	9
Core-trench	$r_2$	$2r_1$	$2r_1$	$2r_1$	$2r_1$	-
Trench's width	$w_{tr}$	$(1,1.5) r_1$	$(1,1.5) r_1$	$(1,1.5) r_1$	$(1,1.5) r_1$	-
Effective area	$A_{eff}(f^i)$	[21]	[47]	[22]	[60]	[39]
Loss coefficient	$\alpha(f^i)$	[21]	[47]	[22]	[60]	[39]
Effective dispersion coefficient	$\beta_{eff}(f^i)$	[21]	[47]	[22]	[60]	[39]
Core pitch [μm]	$\Lambda$	43	51	40	35	-
Core's refractive index	$n_{core}$	1.44	1.44	1.44	1.44	1.44
Bending radius [mm]	$r_b$	144	144	140	140	140

### A. ICXT Analysis in BSDM EONs

According to Fig. 1, four real-world TAWC-MCFs are considered for the BSDM EON, namely, MC04, MC07, MC13, and MC19. Additionally, SSMFs are used in the BuMFPs strategy. The physical optical fiber parameters are listed in Table 1. We considered these MCFs because they are currently manufactured and represent cutting-edge technology in each category. For example, to the best of our knowledge, while several types of standard CD TAWC-MCFs have been introduced in the literature, the 4-core lattice is the optimal layout for this type of MCF. Moreover, concerning the non-standard TAWC-MCFs, hexagonal close-packed MCFs are more efficient based on the core numbers and lower ICXT. In this regard, we adopted the MC07 in [47], which has the lowest ICXT. Furthermore, for MC13 and MC19, we adopted the MCFs introduced in [22,60], respectively. It should be noted that, in contrast to works in the literature, we apply frequency-dependent values of parameters such as loss coefficient, effective area, and effective dispersion coefficient. Therefore, both the GSNR and the ICXT of each channel depend on the frequency. Recently, one of the trends in manufacturing MCFs is the development of ultra-low-ICXT and -loss MCFs that operate across multiple bands, from the C-band to the L-band [17]. The main reason to implement TAWC-MCFs with ultra-low ICXT and loss, especially in long-distance networks, is to increase the transmission bit rate and reduce planning complexity. In the ultra-low-ICXT and -loss working zone, the ICXT in all channels of all cores is lower than the ICXT threshold of the highest modulation format level (i.e., 64QAM) for long-haul distances (even 10,000 km) with a loss coefficient lower than the SSMF [17,35]. To demonstrate this phenomenon, let us first analyze the ICXT in terms of the PCC and MCC based on the ratio of trench width to core radius. Figure 4(a) illustrates the PCC in terms of frequency in the C + L + S-band from solving Eq. (2).

As shown in Fig. 4, the PCC undergoes significant changes based on frequency. Therefore, in a multi-band system, considering the PCC only at 1550 nm is an oversimplification that may lead to large inaccuracies. We can also see that the ICXT depends on the ratio of trench width to core radius, i.e.,  $w_{tr}/r_1$ . By increasing this ratio, the ICXT decreases. However, we cannot increase it indefinitely. The distance between two adjacent

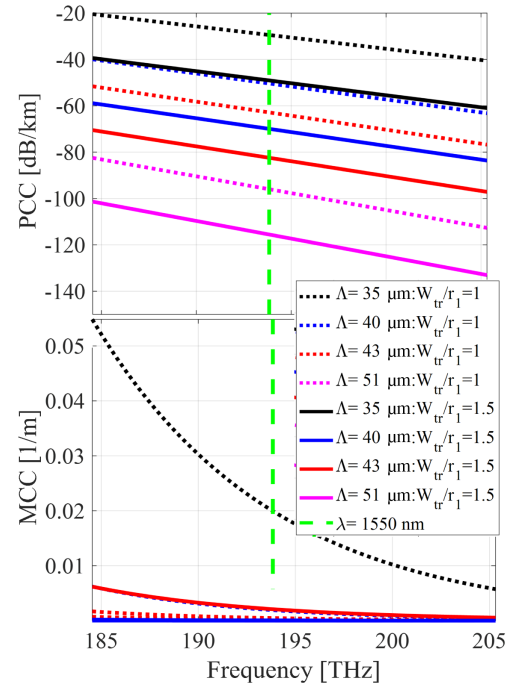


**Fig. 4.** (a) PCC and (b) MCC versus frequency for different values of the ratio of trench width to core radius, i.e.,  $w_{tr}/r_1$  for 4-core MCF (MC04) with  $\Lambda = 43 \mu\text{m}$ , 7-core MCF (MC07) with  $\Lambda = 51 \mu\text{m}$ , 13-core MCF (MC13) with  $\Lambda = 40 \mu\text{m}$ , and 19-core MCF (MC19) with  $\Lambda = 35 \mu\text{m}$ .

trenches must be less than 3 μm [46]; therefore, we can derive Eq. (10) based on Fig. 1:

$$R_{tr} \leq \frac{\Lambda - 3}{2r_1} - 2. \quad (10)$$

For instance, in the case of MC19, this ratio of trench width to core radius cannot exceed 1.5. Therefore, to have a fair comparison we consider  $w_{tr}/r_1 = 1.5$  in the remainder of this paper. As anticipated, the PCC of MC19 is higher compared to other MCFs due to its lower core pitch. The ICXT of MC19 is 22 dB/km higher than MC13, 34 dB/km higher than MC04, and 55 dB/km higher than MC07, with differences in their core pitches being 5 μm, 8 μm, and 16 μm, respectively. Increasing the  $R_{tr}$  by 50% results in approximately a 20 dB

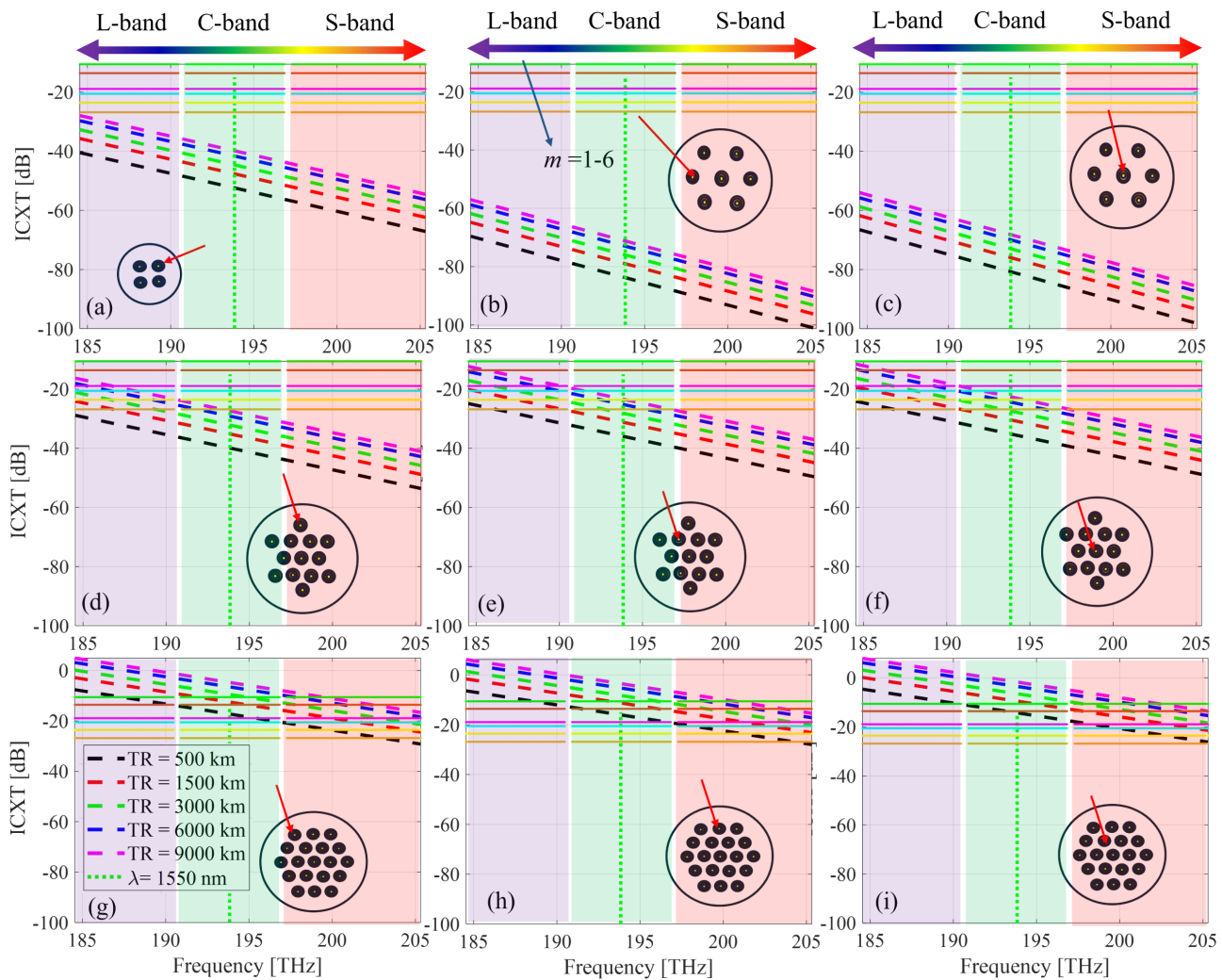


**Fig. 5.** ICXT for (a) MC04; (b), (c) MC07; (d)–(f) MC13; and (g)–(i) MC19 over transmission reaches of 500 km to 9000 km.

decrease in ICXT. The MCC for different values of the ratio of trench width to core radius, calculated using Eq. (3), is illustrated in Fig. 4(b). The results show that by increasing the  $w_{tr}/r_1$  from 1 to 1.5 in an MC19, a significant decrease in MCC occurs. However, increasing it further does not result in any significant change. Regarding other MCFs, the results indicate that changes in  $w_{tr}/r_1$  do not significantly affect the MCC. As we mentioned earlier in the ultra-low-ICXT and -loss regime, for all (connection, channel, core) tuples, the ICXT must be lower than the crosstalk threshold of the highest modulation format level in the network, i.e.,  $\mu_{ICXT_{th}}^m > \mu_{ICXT}$ . According to Eq. (9),  $\mu_{ICXT_{th}}^m$  is  $-10.58, -13.59, -18.93, -20.58, -23.59$ , and  $-26.82$  dB for  $m = 1\text{--}6$ , corresponding to GMI values from 2 to 12 related to  $m = 1\text{--}6$  (see Fig. 5). These values are related to the pre-forward error correction (FEC) BER of  $1.5 \times 10^{-2}$ , and  $\Gamma = 1$  dB. The soft decision FEC with a maximum overhead of 20%–30% is used [41]. Moreover, the GSNR threshold for each modulation format level  $m$  depends on the pre-FEC BER and can be determined from Eq. (7) in [4]. Therefore, the GSNR threshold is 3.71, 6.72, 10.84, 13.24, 16.16, and 19.01 dB for the pre-FEC BER of  $1.5 \times 10^{-2}$ .

The ICXT, as calculated using Eq. (1), is simulated for transmission distances ranging from 500 km to 9000 km using the parameters listed in Table 1. The results presented in Fig. 5 lead to several observations. First, the ICXT of a channel is influenced not only by the transmission distance but also by factors such as frequency, the physical configuration of the MCF, the number of neighboring cores, and the core pitch.

Consider MC04 with a core pitch of 43  $\mu\text{m}$ , depicted in Fig. 5(a). Each core in MC04 has two neighboring cores, rendering it an ultra-low-ICXT MCF. However, from Fig. 5(a) and Fig. 4(a), it is evident that, with  $w_{tr}/r_1 = 1$ , MC04 does not qualify as an ultra-low-ICXT MCF. Despite this, the ICXT in MC07 cores is lower than in MC04 [see Figs. 5(b) and 5(c)]. Although MC07 features two types of cores, inner ones with six neighbors and outer ones with three neighbors, the primary determinant of ICXT is the core pitch, set at 51  $\mu\text{m}$  in MC07. Therefore, MC07 qualifies as an ultra-low-ICXT MCF. Both MC04 and MC07 are also ultra-low-loss MCFs, with loss coefficients lower than those of SSMFs (as reported in [21,47], respectively). Increasing the core count from 7 to 13 results in an increase in ICXT due to the reduction in core pitch. Figures 5(d)–5(f) illustrate the variation in ICXT in MC13,

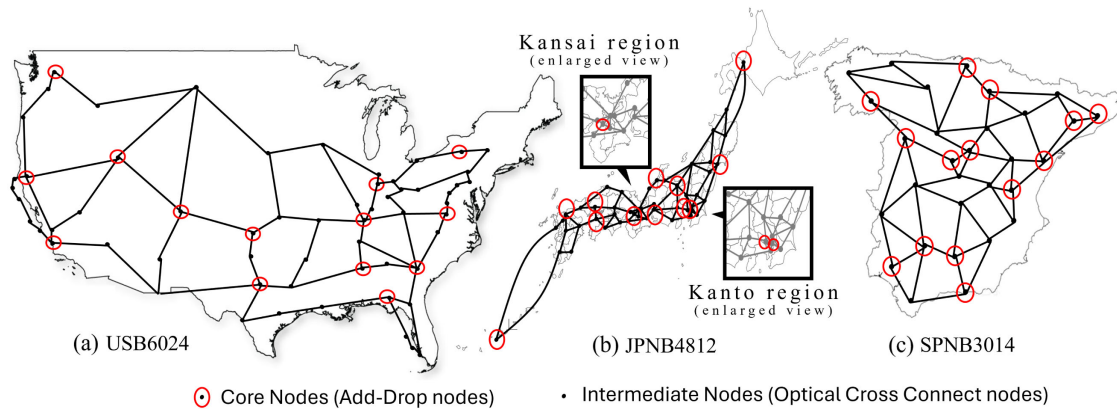


**Fig. 6.** Network topology of the (a) United States backbone (USB6014), (b) Japan backbone (JPN4812), and (c) Spain backbone (SPNB3014).

which, as observed, is not an ultra-low-ICXT MCF. For certain (channel, core) pairs, particularly those in the L-band and lower frequency of the C-band, the modulation format level may need to be lowered to  $m = 6$  in some transmission scenarios. Consequently, not only does the transmission bit rate decrease, but service provisioning becomes more complex, especially in ICXT-aware planning strategies.

Moreover, in the worst-case scenario, i.e., lowest frequency with the highest transmission reach, (channel, core) pairs may only support data transmissions with  $m = 1$ , although this situation does not occur for MC19. Indeed, Figs. 5(g)–5(i) demonstrate that, by increasing the number of cores and reducing the core pitch to 35  $\mu\text{m}$  in MC19, data transmission becomes impractical for certain (channel, core) pairs at higher transmission reaches in most of the C- and L-band resources. This challenge is more pronounced for (channel, core) pairs in the L-band. Therefore, MCFs with core pitch lower than 43  $\mu\text{m}$  are not good candidates for the BSDM EONs such as MC13 and MC19.

## **B. Comparison of Metro-Core Backbone Networks Performance: MCFs versus BuMFPs**

In this section, we investigate two BSDM strategies, namely, MCFs and BuMFPs. However, inspired by the previous discussion, we focus on TAWC-MCFs. To do this, three networks are considered in this study, each with a different size. The first is the United States of America backbone network called USB6014, which has 60 nodes and 79 links, focusing on traffic exchange between the core nodes, i.e., only 14 nodes, as shown in Fig. 6. In the other nodes, we have only optical cross-connects, with add/drop functionality exclusively at the core nodes. The average nodal degree is 2.63, the average link distance is 447 km, and the maximum LP distance for the  $k = 5$  shortest paths is 6493 km. The second network is the Spanish backbone network called SPNB3014, which has 30 nodes and 56 links. The average nodal degree is 3.73, the average link distance is 148.5 km, and the maximum LP distance for the  $k = 10$  shortest paths is 1044 km. The third network is the Japanese backbone network called JPNB4812, which has 48 nodes and 56 links. The average nodal degree is 3.41, the average link distance is 153.7 km, and the average LP distance for the  $k = 10$  shortest paths is 2292 km. To begin with, let

us examine USB6014. We calculate the transmission bit rates for all tuples of (connection, channel, core) for USB6014 operating across the C + L + S-band with 268 channels, each having a bandwidth of 75 GHz. This analysis encompasses 92 connections within the network. The maximum span length is 100 km in each link. The symbol rate of each channel is 64 Gbaud, and the transmission bit rate varies between 100 Gbps and 600 Gbps based on the GSNR of each channel, calculated according to Eq. (4) for the  $k = 1$  shortest path of each connection. The noise figures of the DFA amplifiers are 4.5 dB, 5 dB, and 6 dB in the C-, L-, and S-bands, respectively. The optimum pre-tilted launch power for each span is calculated based on the hyper-accelerated scheme introduced in [38].

The modulation format level profiles for all tuples of (connection, channel, core) are depicted in Figs. 7 and 8 for BuMFP-based BSDM and MCF-based BSDM, respectively. The modulation format is determined as  $\min\{m_{\text{GSNR}}, m_{\text{ICXT}-1 \text{ dB}}\}$ , where  $m_{\text{GSNR}}$  denotes the modulation format level meeting the GSNR threshold, and  $m_{\text{ICXT}-1 \text{ dB}}$  represents the modulation format meeting the ICXT threshold of 1 dB penalty. The comparison between Fig. 7 and Fig. 8 reveals that MC04 and MC07, characterized by lower loss coefficients, exhibit higher modulation format levels. In this study, we pre-calculated the GSNR profiles for all connections

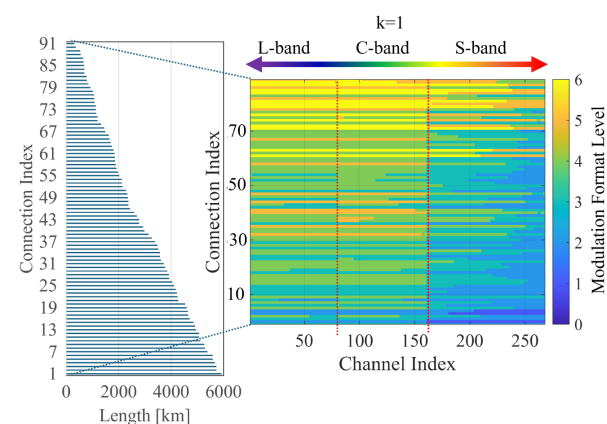


**Fig. 7.** Modulation format level profile (right) and the connection length (left) for USB6014 in the BuMFP scenario and  $k = 1$ .

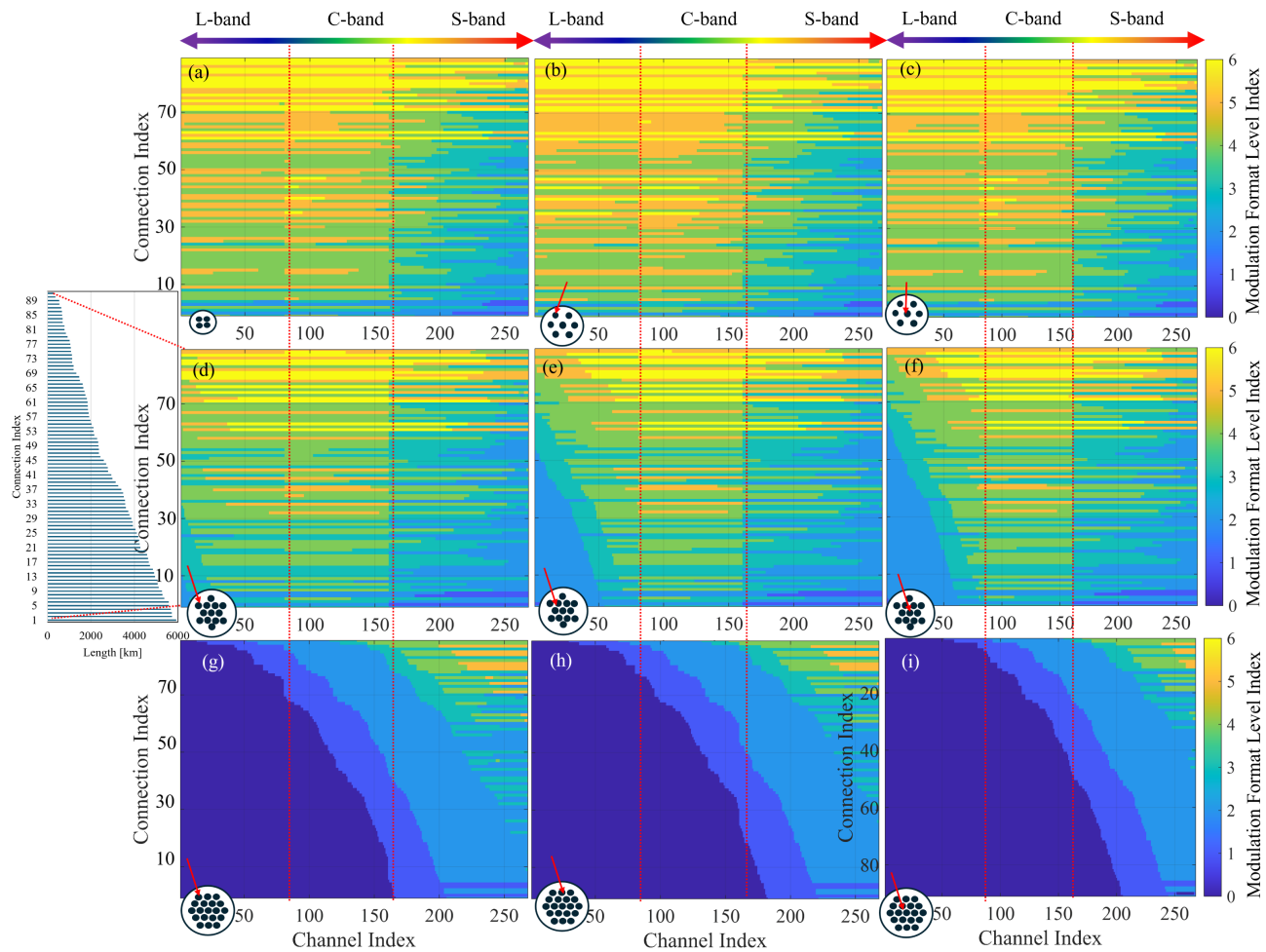


**Fig. 8.** Modulation format level profile for USB6014 in the MCF-based scenario: (a) MC04; (b)/(c) MC07, for cores with 3/6 adjacent neighbors; (d)/(e)/(f) MC13, for cores with 2/5/6 adjacent neighbors; and (g)/(h)/(i) MC19, for cores with 3/4/6 adjacent neighbors.

across the three above-mentioned backbone networks, considering  $k = 5$  for USB6014 (due to longer distances) and  $k = 10$  for the other two networks. However, due to space constraints, we report only the results for USB6014 and  $k = 1$  in this paper. The full dataset, including GSNR profiles for all  $k$  values, is available in [40] for open use in further research.

Accordingly, the loss coefficient appears to be a more prominent factor than the low ICXT, particularly noticeable in the C- and L-bands. The results confirm that increasing the core pitch leads to higher modulation format levels and bit rates, as observed in the results for MC07 compared to others. Additionally, the effect of core pitch is significantly more dominant compared to the number of adjacent cores. For instance, comparing Figs. 8(b) and 8(c) with Fig. 8(a) reveals this dominance. Moreover, decreasing the core pitch in MC13 results in the selection of lower modulation format levels, reducing the capacity per core, as shown in Figs. 8(d)–8(f). This effect is even more pronounced for MC19, where the modulation format level index is zero, indicating that no feasible modulation format can be selected, rendering most of the C- and L-band channels practically unusable [see Figs. 8(g)–8(i)]. To provide a more detailed insight into the capacity performance of MCF-based BSDM and BuMFP-based BSDM, we present

the cumulative throughput of each connection in both BSDM scenarios. Figure 9 illustrates that the capacity performance of ultra-low ICXT and low-loss TAWC-MCFs surpasses that of the BuMFP scenario. This difference is particularly evident in the comparison between MC04 and MF04 (a BuMFP with four SSMF pairs) and between MC07 and MF07 (a BuMFP with seven SSMF pairs), attributable to the lower loss coefficient in the state-of-the-art ultra-low-ICXT and low-loss MC04 and MC07. The extent of this difference depends on the transmission reach and the number of hops for each connection. Increasing the number of cores and decreasing the core pitch enhance the performance of BuMFP-based BSDM. Furthermore, the loss coefficient of MC13 and MC19 is not lower than that of SSMFs due to the lower cladding thickness. However, the throughput degradation in MC13 is relatively minor due to the 40  $\mu\text{m}$  core pitch. In contrast, this degradation is significant for MC19 due to the higher ICXT with a core pitch of 35  $\mu\text{m}$ .

It is worth mentioning that the simulation results for JPNB4812 and SPNB3014 are not illustrated here to save space. However, the simulations exhibit the same behavior as shown in Figs. 7–9. Additionally, the average bit rates per channel for JPNB4812 and SPNB3014 are higher than for

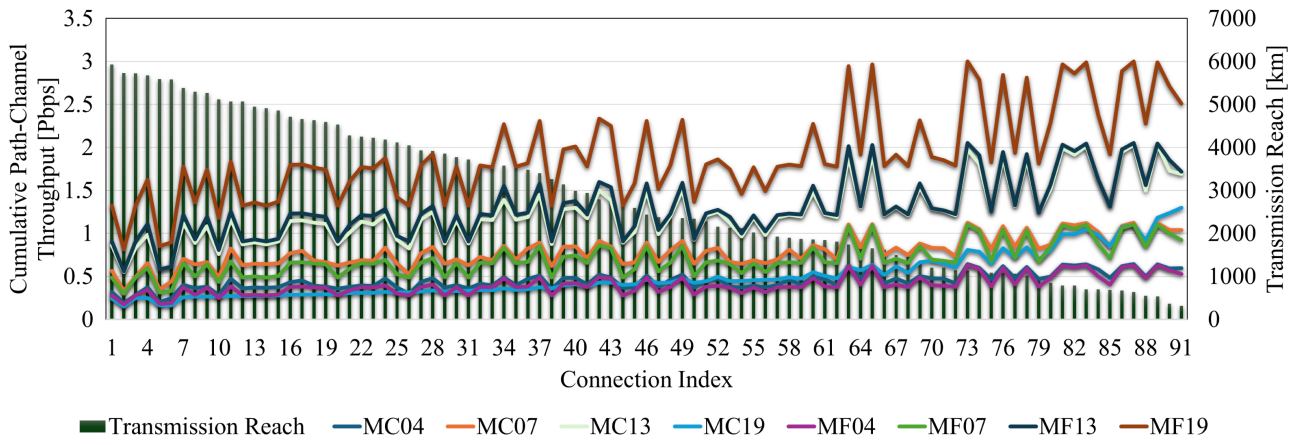


**Fig. 9.** Cumulative (channel-core) throughput [Pbps] in terms of the connections in USB6014 for both BSDM scenarios, i.e., MCF-based (MC04, 07, 13, 19) and BuMFP-based (MF04, 07, 13, 19).

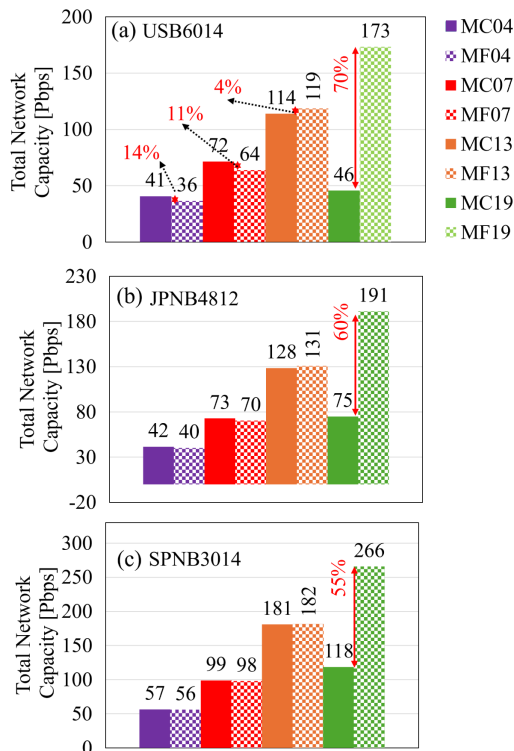


**Fig. 10.** Total network capacity [Pbps] in (a) USB6014, (b) JPNB4812, and (c) SPNB3014 for both BSDM scenarios, i.e., MCF-based (MC04, 07, 13, 19) and BuMFPs-based (MF04, 07, 13, 19).

USB6014 due to the longer-distance connections in the US network. Therefore, in the case of MC19, the number of unfeasible channels in the L-band for SPNB3014 is lower than for JPNB4812, and for both of them, it is lower than for USB6014. The total network capacity for the three topologies is depicted in Fig. 10. We can see the same behavior for all networks. Increasing the number of cores from 4 to 13 results in a linear increase in network capacity, while higher core counts lead to a significant decrease. The results in Fig. 10(a) indicate that MC04 and MC07 exhibit 11% and 14% higher total capacity in USB6014 compared to MF04 and MF07,

respectively. However, for MC13 and MC19, the total network capacity is 4%|73% lower than that of MF13|MF19. These values are 2%|60% and 1%|55% for JPNB4812 and SPNB3014, respectively. Therefore, in scenarios where the core pitch is higher than 40  $\mu\text{m}$ , MCF-based approaches could be comparable to BuMFPs. However, with this core pitch, network planning becomes more complex, requiring ICXT-aware service provisioning (see Fig. 5). Conversely, in ultra-low-ICXT scenarios with a core pitch greater than 43  $\mu\text{m}$ , the modulation format level for all (connection, channel, core) tuples is selected independently of the ICXT value. Finally, the ultra-low ICXT and loss make it a more suitable candidate for the next-gen BSDM backbone EONs. This is because all (connection, channel, core) tuples are feasible for data transmission, and the transmission depends only on the GSNR thresholds, being independent of the ICXT 1 dB penalty due to the MIMO-free transmission.

## 5. CONCLUSIONS

Our study underscores the potential of TAWC-MCF in ultra-high-capacity BSDM backbone EONs. We have demonstrated that MCF-based BSDM EONs, operating in the UL-ICXT and low-loss regime, can provide up to 14% greater network throughput compared to BuMFPs. Through meticulous design of the physical structure of the TAWC-MCF, it is feasible to achieve comparable total network capacity with BuMFPs even with 13 cores and a core pitch of 40  $\mu\text{m}$ . Our results indicate that increasing the number of cores beyond 13 with the limited cladding diameters significantly decreases the total network capacity compared to BuMFPs. Furthermore, our findings suggest that the L-band is not a favorable option for core pitches lower than 43  $\mu\text{m}$ , even for smaller networks like the Spain backbone. Therefore, the C + S-band combination shows greater potential for next-generation BSDM EONs. Overall, TAWC-MCFs with core pitches exceeding 40  $\mu\text{m}$  exhibit promising performance and represent a viable alternative to BuMFPs in broadband optical communication systems. Finally, future research should include comprehensive techno-economic studies to identify the optimal strategy

for upgrading or deploying new optical networks, considering both ULL SMFs and ULL-loss-ICXT MCFs as MCF technology continues to advance.

**Funding.** Universidad Carlos III de Madrid; H2020 Marie Skłodowska-Curie Actions (801538); HORIZON EUROPE Digital, Industry and Space (101096120); Agencia Estatal de Investigación (PID2022-136684OB-C21).

**Acknowledgment.** Farhad Arpanaei acknowledges support from the CONEX-Plus programme funded by Universidad Carlos III de Madrid and the European Union's Horizon 2020 research and innovation programme under the Marie Skłodowska-Curie Actions. The authors would like to acknowledge the support of the EU-funded SEASON project and the Spanish-funded Fun4date-Redes project.

## REFERENCES

1. "The countries fighting for 6G leadership and what they plan for 2030," <https://www.6gworld.com/exclusives/the-countries-fighting-for-6g-leadership-and-what-they-plan-for-2030/>.
2. I. Tomkos, D. Uzunidis, K. Moschopoulos, et al., "The role of optical networking in the 6G era," in *Optical Fiber Communication Conference (OFC)* (2024), paper Tu3B.1.
3. P. Iovanna, A. Bigongiari, F. Cavaliere, et al., "Optical components for transport network enabling the path to 6G," *J. Lightwave Technol.* **40**, 527–537 (2022).
4. F. Arpanaei, J. M. Rivas-Moscoso, I. De Francesca, et al., "Enabling seamless migration of optical metro-urban networks to the multi-band: unveiling a cutting-edge 6D planning tool for the 6G era," *J. Opt. Commun. Netw.* **16**, 463–480 (2024).
5. N. Sambo, C. Castro, N. Costa, et al., "Energy efficiency in next-generation optical networks," in *International Conference on Transparent Optical Networks (ICTON)* (2023), paper Th.B3.1.
6. T. Hoshida, V. Curri, L. Galdino, et al., "Ultrawideband systems and networks: beyond C + L-band," *Proc. IEEE* **110**, 1725–1741 (2022).
7. F. Arpanaei, J. M. Rivas-Moscoso, J. A. Hernández, et al., "Migration strategies from C-band to C+L-band/multi-fiber solutions in optical metropolitan area networks," in *European Conference on Optical Communications (ECOC)* (2023), pp. 1531–1534.
8. W. Klaus, P. J. Winzer, and K. Nakajima, "The role of parallelism in the evolution of optical fiber communication systems," *Proc. IEEE* **110**, 1619–1654 (2022).
9. Y. Yu, L. Xiang, W. Shao, et al., "Numerical estimation of inter-core crosstalk affected by stimulated Raman scattering in weakly coupled multicore fiber," *J. Lightwave Technol.* **42**, 1634–1644 (2024).
10. R. S. Luís, G. Rademacher, B. J. Puttnam, et al., "Crosstalk impact on the performance of wideband multicore-fiber transmission systems," *IEEE J. Sel. Top. Quantum Electron.* **26**, 4400609 (2020).
11. P. J. Winzer, D. T. Neilson, and A. R. Chraplyvy, "Fiber-optic transmission and networking: the previous 20 and the next 20 years," *Opt. Express* **26**, 24190–24239 (2018).
12. M. Klinkowski, P. Lechowicz, and K. Walkowiak, "Survey of resource allocation schemes and algorithms in spectrally-spatially flexible optical networking," *Opt. Switch. Netw.* **27**, 58–78 (2018).
13. K. Nakajima, T. Matsui, K. Saito, et al., "Multi-core fiber technology: next generation optical communication strategy," *IEEE Commun. Stand. Mag.* **1**(3), 38–45 (2017).
14. T. Hayashi and T. Nakanishi, "Multi-core optical fibers for the next-generation communications," *SEI Tech. Rev.* **86**, 23–28 (2018), [https://sumitomoelectric.com/sites/default/files/2020-12/download\\_documents/86-05.pdf](https://sumitomoelectric.com/sites/default/files/2020-12/download_documents/86-05.pdf).
15. P. J. Winzer, "Spatial multiplexing: the next frontier in network capacity scaling," in *European Conference and Exhibition on Optical Communication (ECOC)* (2013), pp. 372–374.
16. T. Matsui, P. L. Pondillo, and K. Nakajima, "Weakly coupled multi-core fiber technology, deployment, and systems," *Proc. IEEE* **110**, 1772–1785 (2022).
17. T. Hayashi, T. Nagashima, T. Morishima, et al., "Multi-core fibers for data center applications," in *European Conference on Optical Communication (ECOC)* (2019).
18. T. Mizuno and Y. Miyamoto, "High-capacity dense space division multiplexing transmission," *Opt. Fiber Technol.* **35**, 108–117 (2017).
19. T. Matsui, Y. Sagae, T. Sakamoto, et al., "Design and applicability of multi-core fibers with standard cladding diameter," *J. Lightwave Technol.* **38**, 6065–6070 (2020).
20. B. J. Puttnam, G. Rademacher, and R. S. Luís, "Space-division multiplexing for optical fiber communications," *Optica* **8**, 1186–1203 (2021).
21. M. Takahashi, K. Maeda, K. Aiso, et al., "Uncoupled 4-core fibre with ultra-low loss and low inter core crosstalk," in *European Conference on Optical Communications (ECOC)* (2020).
22. K. Saitoh and S. Matsuo, "Multicore fibers for large capacity transmission," *Nanophotonics* **2**, 441–454 (2013).
23. T. Matsui, Y. Yamada, Y. Sagae, et al., "Standard cladding diameter multi-core fiber technology," in *Optical Fiber Communication Conference (OFC)* (2021), paper Tu6B.4.
24. X. Mu, A. Ottino, F. M. Ferreira, et al., "Design and transmission analysis of trench-assisted multi-core fibre in standard cladding diameter," *Opt. Express* **30**, 38152–38166 (2022).
25. G. Rademacher, M. van den Hout, R. S. Luís, et al., "Randomly coupled 19-core multi-core fiber with standard cladding diameter," in *Optical Fiber Communication Conference (OFC)* (2023), paper Th4A.4.
26. T. Matsui, T. Sakamoto, Y. Goto, et al., "Design of 125 μm cladding multi-core fiber with full-band compatibility to conventional single-mode fiber," in *European Conference on Optical Communication (ECOC)* (2015).
27. F. Ye, J. Tu, K. Saitoh, et al., "Simple analytical expression for crosstalk estimation in homogeneous trench-assisted multi-core fibers," *Opt. Express* **22**, 23007–23018 (2014).
28. V. I. Kopp, J. Park, J. Zhang, et al., "Ultra-low-crosstalk multicore fiber-integrated pump-signal combiner for a core-pumped EDFA," *Opt. Express* **31**, 16434–16441 (2023).
29. Y. Guan, H. Jiang, M. Gao, et al., "Migrating elastic optical networks from standard single-mode fibers to ultra-low loss fibers: strategies and benefits," in *Optical Fiber Communication Conference (OFC)* (2017), paper W4H.3.
30. Y. Tamura, H. Sakuma, K. Morita, et al., "The first 0.14-dB/km loss optical fiber and its impact on submarine transmission," *J. Lightwave Technol.* **36**, 44–49 (2018).
31. Y. Kujikawa, S. Yoshimoto, M. Ohashi, et al., "The first 0.14-dB/km ultra-low loss optical fiber" (Sumitomo Electric Industries, Ltd., 2017).
32. T. Hyashi, T. Sasaki, and E. Sasaoka, "Behavior of inter-core crosstalk as a noise and its effect on Q-factor in multi-core fiber," *IEICE Trans. Commun.* **E97.B**, 936–944 (2014).
33. B. J. Puttnam, R. S. Luís, G. Rademacher, et al., "319 Tb/s transmission over 3001 km with S, C and L band signals over >120 nm bandwidth in 125 μm wide 4-core fiber," in *Optical Fiber Communication Conference (OFC)* (2021), paper F3B.3.
34. Z. Luo, S. Yin, L. Zhao, et al., "Survivable routing, spectrum, core and band assignment in multi-band space division multiplexing elastic optical networks," *J. Lightwave Technol.* **40**, 3442–3455 (2022).
35. R. S. Luis, B. J. Puttnam, G. Rademacher, et al., "High capacity transmission in low-core count MCFs," in *Signal Processing in Photonic Communications* (2022), paper SpM4I-1.
36. A. Souza, N. Costa, L. Nadal, et al., "Node architectures for high-capacity multi-band over space division multiplexed (MBoSDM) optical networks," in *24th International Conference on Transparent Optical Networks (ICTON)* (2024).
37. L. Nadal, R. Martinez, M. Ali, et al., "Advanced optical transceiver and switching solutions for next-generation optical networks," *J. Opt. Commun. Netw.* **16**, D64–D75 (2024).
38. F. Arpanaei, K. Ghodsifar, H. Beyranvand, et al., "Hyperaccelerated power optimization in multi-band elastic optical networks," in *Optical Fiber Communication Conference (OFC)* (2024), paper Th11.6.
39. P. Poggiolini and M. Ranjbar-Zefreh, "Closed form expressions of the nonlinear interference for UWB systems," in *European Conference on Optical Communication (ECOC)* (2022).

40. F. Arpanaei, "Datasets for ultra-high-capacity band and space division multiplexing backbone EONs: multi-core versus multi-fiber," Zenodo (2024), <https://zenodo.org/records/13759999>.
41. G. Bosco, "Advanced modulation techniques for flexible optical transceivers: the rate/reach tradeoff," *J. Lightwave Technol.* **37**, 36–49 (2019).
42. Open-ROADM-MSA, "Open ROADM MSA device white paper (v13.1)" (Open ROADM MSA GitHub Repository, 2024), [https://github.com/OpenROADM/OpenROADM\\_MSA\\_Public?tab=readme-ov-file](https://github.com/OpenROADM/OpenROADM_MSA_Public?tab=readme-ov-file).
43. Infinera, "The seven vectors of ROADM evolution" (2021), <https://www.infinera.com/wp-content/uploads/The-Seven-Vectors-of-ROADM-Evolution-0302-WP-RevA-1121.pdf>.
44. D. M. Marom, P. D. Colbourne, A. D'errico, et al., "Survey of photonic switching architectures and technologies in support of spatially and spectrally flexible optical networking [Invited]," *J. Opt. Commun. Netw.* **9**, 1–26 (2017).
45. A. Ferrari, D. Pilori, E. Virgillito, et al., "Power control strategies in C+L optical line systems," in *Optical Fiber Communication Conference (OFC)* (2019), paper W2A.48.
46. K. Takenaga, Y. Arakawa, Y. Sasaki, et al., "A large effective area multi-core fibre with an optimised cladding thickness," in *European Conference and Exhibition on Optical Communication* (2011).
47. T. Hayashi, T. Taru, O. Shimakawa, et al., "Uncoupled multi-core fiber enhancing signal-to-noise ratio," *Opt. Express* **20**, B94–B103 (2012).
48. B. Chen, Y. Lei, J. Hu, et al., "Crosstalk-sensitive core and spectrum assignment in MCF-based SDM-EONs," *IEEE Trans. Commun.* **71**, 7133–7148 (2023).
49. Y. Ma, X. Yang, Q. Sun, et al., "Dynamic resource allocation for multicast in SDM-EON: time-decoupled dynamic path cross talk and joint weight," *J. Opt. Commun. Netw.* **15**, 687–699 (2023).
50. J. L. Ravipudi and M. Brandt-Pearce, "Impairment- and fragmentation-aware, energy-efficient dynamic RMSCA for SDM-EONs," *J. Opt. Commun. Netw.* **15**, D10–D22 (2023).
51. Y. Seki, Y. Tanigawa, Y. Hirota, et al., "Core and spectrum allocation to achieve graceful degradation of inter-core crosstalk with generalized hierarchical core prioritization on space-division multiplexing elastic optical networks," *J. Opt. Commun. Netw.* **15**, 43–56 (2023).
52. W. Zheng, M. Yang, C. Zhang, et al., "Evaluation of optical transport unit line-card integration in spatially and spectrally flexible optical networks in terms of device cost and network performance," *J. Lightwave Technol.* **40**, 6319–6330 (2022).
53. F. Arpanaei, B. Shariati, H. Beyranvand, et al., "Physical-layer aware routing, modulation level and resource allocation of SDM networks over FM-MCFs," in *European Conference on Optical Communication (ECOC)* (2019).
54. F. Arpanaei, N. Ardalani, H. Beyranvand, et al., "QoT-aware performance evaluation of spectrally–spatially flexible optical networks over FM-MCFs," *J. Opt. Commun. Netw.* **12**, 288–300 (2020).
55. M. R. Zefreh and P. Poggiolini, "A real-time closed-form model for nonlinearity modeling in ultra-wide-band optical fiber links accounting for inter-channel stimulated Raman scattering and co-propagating Raman amplification," arXiv (2020).
56. Y. Jiang, A. Nespoli, A. Tanzi, et al., "Experimental test of a UWB closed-form EGN model," in *49th European Conference on Optical Communications (ECOC)* (2023).
57. Y. Jiang, G. Bosco, A. Nespoli, et al., "Experimental test of a UWB closed-form EGN model," in *IEEE Photonics Conference (IPC)* (2023).
58. Y. Jiang, A. Nespoli, S. Straullu, et al., "Experimental test of a closed-form EGN model over C+L bands," *J. Lightwave Technol.* (to be published).
59. P. J. Winzer, A. H. Gnauck, A. Konczykowska, et al., "Penalties from in-band crosstalk for advanced optical modulation formats," in *European Conference and Exhibition on Optical Communication* (2011).
60. J. Sakaguchi, B. J. Putnam, W. Klaus, et al., "305 Tb/s space division multiplexed transmission using homogeneous 19-core fiber," *J. Lightwave Technol.* **31**, 554–562 (2013).